DOI: 10.1002/((please add manuscript number))
Article type: Communication

Thermodynamically stable synthesis of large-scale and highly-crystalline transition metal dichalcogenide monolayers and their unipolar n-n heterojunction devices

Juwon Lee, Sangyeon Pak, Paul Giraud, Young-Woo Lee, Yuljae Cho, John Hong, A-Rang Jang, Hee-Suk Chung, Hu Young Jeong, Hyun Suk Shin, Luigi G. Occhipinti, Stephen M. Morris, SeungNam Cha, Jung Inn Sohn*, Jong Min Kim*

J. W. Lee, S. Pak, P. Giraud, Dr. Y. -W. Lee, Y. Cho, J. Hong, Dr. A. -R. Jang, Dr. L. G. Occhipinti, Prof. S. M. Morris, Prof. S. Cha, Dr. J. I. Sohn
Department of Engineering Science, University of Oxford, Parks Road, Oxford, OX1 3PJ, United Kingdom
Email: seungnam.cha@eng.ox.ac.uk; junginn.sohn@eng.ox.ac.uk

Dr. H. -S. Chung
Jeonju center, Korea Basic Science Institute, Jeonju, Jeollabuk-do 54907, Republic of Korea

Prof. H. Y. Jeong
UNIST Central Research Facilities (UCRF), Ulsan National Institute of Science and Technology (UNIST), 50 UNIST-gil, Ulsan, 44919, Republic of Korea

Prof. H. S. Shin
Department of Chemistry, Ulsan National Institute of Science and Technology (UNIST), 50 UNIST-gil, Ulsan 44919, Republic of Korea

Dr. L. G. Occhipinti, Prof. J. M. Kim
Electrical Engineering Division, Engineering Department, University of Cambridge, 9 JJ Thomson Avenue, Cambridge, CB3 0FA, United Kingdom

Keywords: transition metal dichacogenides, two-dimensional materials, chemical vapor deposition, heterojunctions, photodetectors

Abstract

Transition metal dichalcogenide (TMDC) monolayers are considered to be potential materials for atomically thin electronics due to their unique electronic and optical properties. However, large-area and uniform growth of TMDC monolayers with large grain sizes is still a considerable challenge. This report presents a simple but effective approach for large-scale and highly-crystalline molybdenum disulfide monolayers using a solution-processed precursor deposition. The low supersaturation level, triggered by the evaporation of an extremely thin precursor layer, reduces the nucleation density dramatically under a thermodynamically stable condition, yielding uniform and clean monolayer films and large crystal sizes up to 500 μm. As a result, the photoluminescence exhibits only a small full-width-half-maximum of 48 meV, comparable to that of exfoliated and suspended monolayer crystals. It is confirmed that this growth procedure can be extended to the synthesis of other TMDC monolayers, and robust MoS_2/WS_2 heterojunction devices have been easily prepared using this synthetic procedure due to the large-sized crystals. The heterojunction device shows a fast response time (~45 ms) and a significantly high photoresponsivity (~40 AW^{-1}) because of the built-in potential and the majority carrier transport at the n-n junction. These findings indicate an efficient pathway for the fabrication of high-performance two-dimensional optoelectronic devices.

Atomically thin transition metal dichalcogenides (TMDCs) have drawn tremendous attention due to their great potential in a range of nanoelectronic devices such as transistors,[1-4] photodetectors,[5-8] and memory elements.[9-12] It has been known that the electrical and optical properties of TMDC devices are influenced by the number of layers and the grain boundaries.[13-16] Accordingly, numerous studies have focused on developing scalable synthetic schemes for the production of TMDC monolayer films with large-sized crystals, using a variety of growth techniques such as thermolysis,[17-19] pulsed laser deposition,[20-22] the sulfurization of metal or metal oxide films,[23-25] and chemical vapor deposition (CVD).[16,26-28] Among these methods, CVD has been shown to be the most practical method for synthesizing highly-crystalline TMDC monolayers, exhibiting relatively good optical and electrical properties.[16,29] However, it is still a challenge to grow large-scale TMDC monolayer films with a large single-crystalline domain size that is suitable for practical devices.

Most of the CVD processes used for growing TMDC monolayers have involved the use of a solid transition metal oxide powder as a precursor (e.g. MoO_3), and it has been shown that controlling the nucleation reaction at the initial growth stage is one of the important factors for obtaining a large domain size.[26,30-31] For example, some research groups have tried to induce nucleation and growth by placing the growth substrate upside down directly towards the MoO_3 powder.[16,26,32-34] With this powder-based approach, however, it is not easy to obtain a uniform large-area monolayer film reproducibly because of the limited control over the nucleation density, resulting from fast kinetic reactions at a high temperature, and the non-uniform distribution of the MoO_3 powder. As a result, clean monolayer crystals tend to grow only in a specific area where the MoO_3 vapor concentration is relatively low (e.g. at the sides of the substrates).[16,33,35] For this reason, there have been many alternative attempts to control the nucleation density by placing the growth substrate away from the precursor,[30,36-40] or adjusting oxygen flow,[41] argon flow,[42] growth temperature,[43-44] and the furnace position during the

growth process.[31] However, they all have resulted in a non-uniform and position-dependent crystal quality, a relatively small crystal size, low coverage, or a contaminated film. From this perspective, it is highly desirable to develop a new growth protocol in order to achieve precise control over the nucleation density even at a high temperature for synthesizing large-scale, high crystalline, and uniform TMDC monolayers.

Here we present a novel method to synthesize a uniform, large-area TMDC monolayer film with large-sized single-crystal grains via solution-processed precursor deposition. Using this method, a thin precursor film with an extremely small amount of MoO_3 (~0.01 mg) has been prepared on the source substrate, which induces low supersaturation and hence reduces nucleation density dramatically down to 32 nuclei mm^{-2} over the whole substrate surface under the thermodynamically stable condition even at a high temperature around 800°C. As a result, a highly-crystalline and centimeter-scale MoS_2 monolayer has been grown directly on the SiO_2 substrates, and single crystals with a large size up to 500 μm have been easily observed over the substrate. We find that the TMDC monolayer possesses an excellent optical quality with a very small full-width-half-maximum (FWHM) of ~48 meV, which is comparable to or even better than that of exfoliated and suspended single crystal TMDC monolayers. It is also confirmed that our growth strategy can be extended to the growth of other TMDC monolayers such as WS_2, and that it can be used to fabricate robust TMDC heterostructure devices due to the large crystal size. The MoS_2/WS_2 heterostructure devices, based on our synthesis, show rectifying properties and exhibit a faster photoresponse of ~45 ms than that observed for single TMDC monolayer photodetectors because of a built-in potential at the heterojunction. In addition, a considerably higher photoresponsivity of ~40 AW^{-1}, compared to the minority-carrier dominant p-n junction devices using TMDC monolayers, is achieved due to the high photogain from the majority carrier transport of the unipolar n-n heterojunction.

The synthesis of the MoS_2 monolayer was performed by using MoO_3 and sulfur as the precursors. Instead of using a solid powder precursor, we devised an easy and economical method for solution-processed precursor deposition so as to induce a relatively very low supersaturation state from the vapor reactants, leading to a reduced nucleation density, which is essential for large-sized crystal growth.[45-46] MoO_3 powder rarely dissolves in water and exhibits a white opaque color, however, it is highly soluble in ammonium hydroxide (NH_4OH) (**Figure 1**a). The dissolved precursor solution in NH_4OH was then spincoated on the SiO_2 substrate (Figure 1b). Figure 1c and Figure S1a clearly show that the deposited MoO_3 film exhibits a uniform and single color contrast in comparison with the blank SiO_2 substrate. The roughness of the film was less than 1 nm, which indicates the formation of a uniform film thickness (Figure S1b). The weight of the deposited film was calculated to be ~0.01 mg from the thickness measured by atomic force microscopy (AFM) and the density of MoO_3 (Figure S1c,d). It is worth noting that the amount of MoO_3 precursor in our work was 2-3 order of magnitude lower and much more uniformly distributed than that of solid precursors that are typically used in other reports,[16,30] which makes the precursor vapor concentration significantly low during the growth.

The CVD process was conducted in a quartz tube using a furnace under atmospheric pressure as shown in Figure 1d. The growth temperature was raised to 800°C, much higher than that used in previous reports,[16,26,28,47] in order to maximize the crystal size compared to lower temperature growth (Figure S2). The sublimed sulfur was transported downstream by the Ar carrier gas, and then sulfurized precursor molecules induce a supersaturation state around the substrate, which results in the nucleation of MoS_2. At this stage, it is important to note that the extremely small amount of precursor in the solution-processed thin film makes the supersaturation level significantly low near the substrate, which leads to a very low nucleation density on the surface (Figure 1e). With the significantly low nucleation density, the growth of

the MoS_2 monolayer diffuses extensively along the surface with little disturbance from neighboring crystals. As a result, a uniform centimeter-scale MoS_2 monolayer film has been obtained with a growth time of 5 min as shown in Figure 1f. While the continuous MoS_2 monolayer film was found on the center of the substrate (Figure 1g), large triangular crystals with a size ranging from 200 to 400 μm were found to meet each other to form interconnected shapes on the edges of the substrate where the flow of the precursor was not sufficient (Figure 1h). The size of the largest triangular crystals reached up to 500 μm (Figure 1i).

To identify whether the crystal size could be enlarged, we increased the growth time up to 30 min (Figure S3). However, the size of the crystals observed on the edge was almost within the same range as those grown for 5 min. Interestingly, the monolayer film was rarely contaminated by additional nucleation or growth upon the crystals even during the relatively long growth time. Furthermore, the grain size was also similar to that of the crystals on the edge, even though grain boundaries were observed in some parts of the film, which might be associated with a grain boundary uplifting phenomenon frequently found when using long growth times or high precursor concentration.[48] These results indicate that our growth process was almost completed within a 5 min period, without any overgrowth due to a small precursor supply, therefore, the crystals were rarely contaminated by the additional growth time even at the center of the substrate where the supersaturation level is expected to be at its highest. On the contrary, when a powder MoO_3 precursor (10 mg) was used for the growth, noticeable contamination was found at the center of the substrate by the bombardment of small particles that nucleated on the surface of the crystals (Figure S4). Collectively, these results show that our growth method is insensitive to the growth time, which can be advantageous for practical applications.

The quality of the monolayer MoS_2 film was characterized by AFM, Raman spectroscopy, and Photoluminescence (PL) spectroscopy. **Figure 2**a shows a typical AFM topography image of the MoS_2 crystal grown in our work. The height profile shows that the thickness of the MoS_2

crystal is around 0.8 nm (Figure 2a), corresponding to a MoS_2 monolayer. The Raman spectrum also demonstrates that the frequency difference between the E^1_{2g} and A_{1g} peak is ~18.8 cm^{-1} (Figure 2b), which is a clear signature of a monolayer of MoS_2. It is well-known that the quality of the crystal can be clearly assessed using PL measurements. Figure 2c shows the PL intensity normalized to the intensity of the A_{1g} Raman peak. Noticeably, the PL intensity of the monolayer grown from the solution-processed precursor deposition is more than 35 times more intense than that observed for the monolayer fabricated using the solid powder-based growth process (Figure S5). The FWHM was found to be as small as 48 meV, which is similar to or in some cases better than that of exfoliated and suspended crystals.[13,49] The distinct difference in optical properties can be explained by the additional nucleation and crystal growth, which can be easily initiated under a high supersaturation condition when using a relatively large amount of precursor.[29,31-32,50] However, with an extremely small amount of precursor, a continuous crystal growth is preferred instead of multiple nucleation sites because the low supersaturation level limits additional nucleation processes. Therefore, the crystals grown in a low supersaturation environment exhibit a very clean surface, and that is why they show much clearer and sharper spectra in the Raman and PL measurements, which is indicative of a high-quality monolayer. Figure 2d also reinforces this finding as it shows the Raman mapping images for the E^1_{2g} and A_{1g} peak along with a PL mapping image at 667 nm, highlighting that a single crystal exhibits a good uniformity.

Furthermore, to assess the homogeneity of the MoS_2 monolayer film over the whole substrate, Raman spectra were also taken at 50 different locations on the substrate (inset of Figure 2e). The statistical values as a function of position were plotted in Figure 2e. The standard deviation of the Raman frequency difference between the E^1_{2g} and A_{1g} peaks was significantly small (0.3 cm^{-1}) with an average of 19.1 cm^{-1}. The FWHM of the E^1_{2g} peak also showed a small variation of 0.16 cm^{-1} with an average of 3.5 cm^{-1}. This trend was found to be even more strikingly in the

PL spectra (Figure 2f). The position of the PL peaks was found to be almost the same at 1.86 eV over the entire substrate, and the FWHM did not change from the 50 meV value. These results clearly highlight the uniformity of our monolayer film over the entire substrate.

The crystal structure of the MoS_2 monolayer was observed directly using high-resolution TEM, selected area electron diffraction (SAED), and annular dark-filed scanning transmission electron microscopy (ADF-STEM). The MoS_2 crystals transferred on a gold grid show the clear surface and well-organized honeycomb structure, and the corresponding hexagonal symmetrical SAED pattern confirms that the MoS_2 sample is indeed a single-crystal (Figure 2g). The ADF-STEM image also clearly shows the atomic model of MoS_2 along with the spatial distribution of the Mo and S atoms (Figure 2h). These findings also suggest that our sample has been grown with a high crystalline quality.

To further investigate the effect of the supersaturation level on the monolayer growth, the synthesis was carried out with various solution-processed precursor films deposited using different concentrations of the MoO_3 solution. The growth process was performed using a similar process to that described above, except that the growth time was reduced to 3 min to investigate the grain size more clearly before the crystals merge with each other. By controlling the precursor amount from 0.001 to 1 mg, we clearly observed the effect of the supersaturation level on the nucleation density and the grain size. **Figure 3**a-e shows the optical images in the center of the substrate from each growth experiment. For a precursor amount of 0.001 mg, crystals with a size ranging from 10 to 30 μm were found to be distributed very sparsely over the substrate, and the nucleation density was found to be only 9 mm^{-2} (Figure 3f). As the precursor amount increased to 0.01 mg, the nucleation density and the average crystal size also gradually rose to ~32 mm^{-2} and ~300 μm, respectively. However, this growth trend was significantly altered above a precursor amount of 0.01 mg. The crystal size was reduced to 30 μm when the precursor amount was increased to 0.1 mg, yet the nucleation density was found

to be very high, greater than 1,200 mm^{-2}. Finally, when the precursor amount reached 1 mg, we found that the center of the substrate was completely contaminated from a much higher nucleation density that resulted from the smaller MoS_2 particles that were less than 1 μm because of the large supply of precursor and the high reactant accumulation. It is worth noting that the average coverage and the nucleation density increase with the amount of MoO_3, however, the size of the crystal is the largest at an amount of 0.01 mg. From these results, it is proposed that there are two distinct dominant growth regimes with a transition point around 0.01 mg. For an extremely low precursor concentration, the low supersaturation leads to a relatively low nucleation rate, which guarantees that thermodynamically stable reactions occur dominantly during the growth.[33,51] In a thermodynamically favored process, reactive atoms have enough time to diffuses to energetically favorable locations, leading to the formation of a stable and high-crystalline structure, which is known to be a triangular shape in our case. It was confirmed that the shape of all the crystals grown below a precursor amount of 0.01 mg was almost right-triangular due to the thermodynamically stable condition being satisfied. On the other hand, a large amount of precursor above 0.01 mg causes a higher supersaturation level and a much faster nucleation process, resulting in reaction instability. As a result, the crystal growth process is dominated mainly by a kinetic-controlled reaction process rather than a thermodynamically stable process.[33,51] In the kinetic-controlled regime, it is not easy for Mo and S atoms to diffuse to the energetically favorable sites because of the high reaction rate. Therefore, the size of the crystals became very small in this regime. In addition, the shape of the grown crystals was less triangular in shape, and instead truncated triangles or round-shaped domains were formed. These findings suggest that large-scale and highly crystalline TMDC monolayers can be achieved under the thermodynamic-controlled regime by balancing the nucleation and growth rates during the synthesis process.

Our proposed strategy to control the nucleation density for large single crystals and promote crystal growth under a thermodynamically stable condition can be generalized to other TMDC monolayers such as WS_2 (Figure S6). As a result, this can facilitate the fabrication of not only homogeneous device arrays but also robust heterostructure devices by virtue of the large-sized crystals. A few studies have been reported on p-n junction photodetectors that focused on improving the slow response time of two-dimensional monolayer photodetectors.[52-56] However, in each case, they have all sacrificed the high photosensitivity of the TMDC monolayer and showed a very low photoresponsivity much less than that of Si-based photodetectors (< 1 AW^{-1}) because of the short carrier lifetimes caused by minority carrier transport. To avoid this issue, we have employed unipolar n-n heterojunctions that are based on majority carrier transport processes so as to maintain the high photoresponsivity of the TMDC monolayer as well as to improve the response time. After synthesizing both of the MoS_2 and WS_2 monolayers with large-sized crystals, the WS_2 monolayer was then transferred onto the top of the MoS_2 monolayer as shown in **Figure 4**a,b. The Raman spectrum at the junction shows the typical vibration modes of both the MoS_2 and WS_2 monolayers together (Figure 4c). Interestingly, the out-of-plane A_{1g} peak of WS_2 on the overlapped layers became noticeably stronger than that on the monolayer and blue-shifted for 1.7 cm^{-1} due to the stiffness of the vibration mode by increasing the number of layers.[57] On the other hand, the intensity of each PL peak became remarkably weak on the heterostructure (Figure 4d). The PL intensity reduction can be attributed to the transition towards an indirect band gap due to an increase in the thickness, similar to that found in single TMDC layers, or the efficient exciton dissociation at the junction because of the built-in potential of the type II heterostructure.[58-60]

Figure 4e,f shows that the I-V curves of the MoS_2/WS_2 heterostructure device exhibit rectifying behavior due to the type II junction. The on/off ratio could be controlled by a gate voltage and reached up to around 500 at a gate voltage of -10 V. However, the channel was thoroughly

depleted under -30 V. When the heterojunction forms a type-II junction, some electrons are transferred from WS_2 to MoS_2 (Figure 4g). Unlike p-n junctions, the transfer of holes occurs relatively less as both monolayers have n-type semiconducting properties. The transferred electrons leave behind an electron depletion region in WS_2, and develop an electron accumulation region in MoS_2, resulting in the formation of a built-in potential between the junction (Figure 4h). When a positive bias is applied, both the electron depletion region and the electron accumulation region decrease and the built-in potential across the junction region also decreases, making it much easier for electrons to pass the junction. On the contrary, the built-in potential increases and much less electrons can then overcome the barrier under a negative bias.

Figure 4i shows the photoresponse of our device at forward bias (V_{DS} = 3 V) in time domain with blue laser light (λ = 450 nm). The photoresponsivity (R) of the device at forward bias, estimated by the equation $R = I_{ph}/P$, where I_{ph} is the photocurrent and P is the absorbed laser power, was found to be significantly high at ~178 A/W even at zero gate bias. However, the response time was extremely slow at τ_{rise} = 30 s, which is the phenomena commonly observed in single MoS_2 monolayer photodetectors.[5,61] It is known that the photoresponse dynamics of 2D materials are significantly affected by the surroundings such as underlying substrates and gas molecules from the environment.[5,62] These surrounding factors induce trap states in the monolayer, which cause a slow response time in single TMDC monolayer photodetectors (Figure S7), yet at the same time contribute to a large photogain due to the prolonged recombination time.[61] As the small potential barrier in our device almost vanishes at forward bias, the carriers released from the trap sites by incident photons can flow through the channel even after the incident light is turned off. Therefore, our device at forward bias operates similarly to single TMDC monolayer photodetectors with a long response time.

A different trend was observed in the photoresponse at reverse bias as shown in Figure 4j. The photoresponse became much faster with a rise time of 45 ms (Figure 4k). Even though the photoresponsivity decreased to ~40 AW^{-1}, it is still much higher than that of the p-n junction photodiodes based upon TMDC monolayers.[52-56] The photogain (*G*), the ratio of collected electrons to photon absorbed per second, can be calculated to be higher than 18, even when assuming that the absorption rate of the photons is 100%. The high photoresponsivity is thought to originate from the high photogain. A photogain greater than unity is not usually observed in p-n junction type photodetectors because the minority carrier transport dominates the device, which makes carrier lifetime short. The results from our devices at reverse bias show that the n-n TMDC monolayer heterostructure photodetectors can significantly improve the response time, while maintaining the photoresponsivity at a considerably high level; this is because the operation of our device is based upon the majority carrier transport in the n-n heterojunction where the carrier lifetime is relative long compared to that of a conventional p-n junction.

In conclusion, large-scale and highly-crystalline MoS_2 monolayer films have been directly synthesized on a SiO_2 substrate using solution-processed precursor deposition. The relatively small amount of metal oxide precursor creates a low supersaturation level, and thus reduces nucleation density, which in turn facilitates the growth of large-sized and highly-crystalline crystals under a thermodynamically stable reaction condition. This strategy can be easily applied to other TMDC monolayers such as WS_2, and makes it possible to fabricate robust TMDC heterostructure devices due to large sized crystals. Specifically, the unipolar n-n MoS_2/WS_2 heterojunction device exhibits an improved response time, which is one of the drawbacks when using TMDC monolayer photodetectors, without losing the high photoresponsivity of the TMDC monolayer due to majority carrier transport. The current findings are of significant importance in the utilization of TMDC monolayers for future electronic and optoelectronic devices.

Experimental Section

Preparation of MoO_3 film: MoO_3 powder (200 mg, Sigma Aldrich) was added to NH_4OH (10 ml) in a small vial to produce a 20 mg/ml concentration of MoO_3 solution. The solution was sonicated and stirred for more than 10 min so as to dissolve the powder completely. A MoO_3 film was spincoated with a drop of solution at 3000 rpm for 1 min on a SiO_2 substrate that was treated with oxygen plasma for 10 min. The deposited MoO_3 film was then annealed at 300°C for 10 min before the growth in order to remove the solvent completely. The deposited amount of MoO_3 was around 0.01 mg as explained in the manuscript and Supporting Information. When comparing the effect of the precursor amount in Figure 3, the MoO_3 films were deposited by just dropping 10 μg of a specific concentration of MoO_3 solution ranging from 0.1 to 100 mg/ml, instead of using spincoating, in order to control the deposited amount precisely.

CVD growth of MoS_2 monolayer: A SiO_2 substrate with a MoO_3 film deposited by the solution-processed method was used as a source substrate. The source substrate was placed in an alumina crucible in the middle of the 50-mm quartz tube. The growth substrate was loaded upside down above the crucible. Another crucible containing 50 mg of sulfur powder (Sigma Aldrich) was placed upstream. The CVD growth was then performed at atmospheric pressure with a continuous flow of pure argon gas. The temperature of the furnace was raised to 300°C and remained for 20 min under 1,000 sccm flow of argon gas to remove oxygen and water in the tube, and then increased to 800 °C at a rate of 20 °C/min with 150 sccm of argon. The sulfur gas was introduced when the temperature of the furnace approached ~720°C. The growth was done for 5 min for the MoS_2 monolayer film, and the furnace was then cooled to room temperature.

MoS_2/WS_2 heterostructure device fabrication: The MoS_2/WS_2 heterojunction devices were fabricated by transferring the WS_2 monolayer on top of the MoS_2 monolayer. The polymethyl methacrylate (PMMA) liquid was spincoated onto the substrate with the WS_2 monolayers at

3000 rpm for 1 min. The substrate was annealed at 120°C for 10 min and was soaked into a 1M KOH solution. After the PMMA film with the WS_2 monolayer film was separated from the SiO_2 substrate, it was floated on clean water to cleanse the film. Transferring the WS_2 monolayer on top of the MoS_2 monolayer was done in ethanol because soaking TMDC monolayers in water can result in breaking of the monolayer films. After the PMMA was dissolved by acetone and washed by ethanol, a stacked MoS_2/WS_2 heterojunction device was obtained. The electrodes were formed on each monolayer and were drawn parallel with the junction. For better contact, the heterojunction device was annealed before the measurement to completely remove water molecules which might exist between the junction or on the substrate.

Supporting Information
Supporting Information is available from the Wiley Online Library or from the author.

Acknowledgements

This research was supported by the European Research Council under the the European Union's Seventh Framework Programme (FP/2007-2013)/Grant Agreement no. 340538 (Project 'UniQDS') and no. 685758 (Project '1D-NEON'). In addition, S.M.M. would also like to thank The Royal Society for financial support.

Received: ((will be filled in by the editorial staff))
Revised: ((will be filled in by the editorial staff))
Published online: ((will be filled in by the editorial staff))

References

[1] B. Radisavljevic, A. Radenovic, J. Brivio, V. Giacometti, A. Kis, *Nat. Nanotechnol.* **2011**, 6, 147.

[2] B. Radisavljevic, A. Kis, *Nat. Mater.* **2013**, 12, 815.

[3] J. Wang, Q. Yao, C. W. Huang, X. Zou, L. Liao, S. Chen, Z. Fan, K. Zhang, W. Wu, X. Xiao, C. Jiang, W. W. Wu, *Adv. Mater.* **2016**, 28, 8302.

[4] X. Li, L. Yang, M. Si, S. Li, M. Huang, P. Ye, Y. Wu, *Adv. Mater.* **2015**, 27, 1547.

[5] O. Lopez-Sanchez, D. Lembke, M. Kayci, A. Radenovic, A. Kis, *Nat. Nanotechnol.* **2013**, 8, 497.

[6] W. Zhang, J. K. Huang, C. H. Chen, Y. H. Chang, Y. J. Cheng, L. J. Li, *Adv. Mater.* **2013**, 25, 3456.

[7] X. Wang, P. Wang, J. Wang, W. Hu, X. Zhou, N. Guo, H. Huang, S. Sun, H. Shen, T. Lin, M. Tang, L. Liao, A. Jiang, J. Sun, X. Meng, X. Chen, W. Lu, J. Chu, *Adv. Mater.* **2015**, 27, 6575.

[8] Z. Yin, H. Li, H. Li, L. Jiang, Y. Shi, Y. Sun, G. Lu, Q. Zhang, X. Chen, H. Zhang, *ACS Nano* **2012**, 6, 74.

[9] D. Lee, E. Hwang, Y. Lee, Y. Choi, J. Kim, S. Lee, J. Cho, *Adv. Mater.* **2016**, 28, 9196.

[10] M. Chen, H. Nam, S. Wi, G. Priessnitz, I. Gunawan, X. Liang, *ACS Nano* **2014**, 8, 4023.

[11] M. Choi, G.-H. Lee, Y.-J. Yu, D.-Y. Lee, S. Lee, P. Kim, J. Hone, W. Yoo, *Nat. Commun.* **2013**, 4, 1624.

[12] J. Lee, S. Pak, Y.-W. Lee, Y. Cho, J. Hong, P. Giraud, H. Shin, S. M. Morris, J. Sohn, S. Cha, J. Kim, *Nat. Commun.* **2017**, 8, 14734.

[13] K. F. Mak, C. Lee, J. Hone, J. Shan, T. F. Heinz, *Phys. Rev. Lett.* **2010**, 105, 136805.

[14] H. Lee, S.-W. Min, Y.-G. Chang, M. Park, T. Nam, H. Kim, J. Kim, S. Ryu, S. Im, *Nano Lett.* **2012**, 12, 3695.

[15] S.-W. Min, H. Lee, H. Choi, M. Park, T. Nam, H. Kim, S. Ryu, S. Im, *Nanoscale* **2012**, 5, 548.

[16] A. M. van der Zande, P. Y. Huang, D. A. Chenet, T. C. Berkelbach, Y. You, G.-H. Lee, T. F. Heinz, D. R. Reichman, D. A. Muller, J. C. Hone, *Nat. Mater.* **2013**, 12, 554.

[17] K.-K. Liu, W. Zhang, Y.-H. Lee, Y.-C. Lin, M.-T. Chang, C.-Y. Su, C.-S. Chang, H. Li, Y. Shi, H. Zhang, C.-S. Lai, L.-J. Li, *Nano Lett.* **2012**, 12, 1538.

[18] J. Yang, Y. Gu, E. Lee, H. Lee, S. Park, M.-H. Cho, Y. Kim, Y.-H. Kim, H. Kim, *Nanoscale* **2015**, 7, 9311.

[19] A. S. George, Z. Mutlu, R. Ionescu, R. J. Wu, J. S. Jeong, H. H. Bay, Y. Chai, A. K. Mkhoyan, M. Ozkan, C. S. Ozkan, *Adv. Funct. Mater.* **2014**, 24, 7461.

[20] M. I. Serna, S. H. Yoo, S. Moreno, Y. Xi, J. Oviedo, H. Choi, H. N. Alshareef, M. J. Kim, M. Minary-Jolandan, M. A. Quevedo-Lopez, *ACS Nano* **2016**, 10, 6054.

[21] J. D. Yao, Z. Q. Zheng, J. M. Shao, G. W. Yang, *Nanoscale* **2015**, 7, 14974.

[22] T. A. J. Loh, D. H. C. Chua, A. T. S. Wee, *Sci. Rep.* **2015**, 5, 18116.

[23] G. Tai, T. Zeng, J. Yu, J. Zhou, Y. You, X. Wang, H. Wu, X. Sun, T. Hu, W. Guo, *Nanoscale* **2015**, 8, 2234.

[24] A. Tarasov, P. M. Campbell, M. Y. Tsai, Z. R. Hesabi, J. Feirer, S. Graham, J. W. Ready, E. M. Vogel, *Adv. Funct. Mater.* **2014**, 24, 6389.

[25] Y.-C. Lin, W. Zhang, J.-K. Huang, K.-K. Liu, Y.-H. Lee, C.-T. Liang, C.-W. Chu, L.-J. Li, *Nanoscale* **2012**, 4, 6637.

[26] Y. H. Lee, X. Q. Zhang, W. Zhang, M. T. Chang, C. T. Lin, K. D. Chang, Y. C. Yu, J. Wang, C. S. Chang, L. J. Li, T. W. Lin, *Adv. Mater.* **2012**, 24, 2320.

[27] S. Najmaei, Z. Liu, W. Zhou, X. Zou, G. Shi, S. Lei, B. I. Yakobson, J.-C. Idrobo, P. M. Ajayan, J. Lou, *Nat. Mater.* **2013**, 12, 754.

[28] D. Dumcenco, D. Ovchinnikov, K. Marinov, P. Lazić, M. Gibertini, N. Marzari, O. Sanchez, Y.-C. Kung, D. Krasnozhon, M.-W. Chen, S. Bertolazzi, P. Gillet, A. i Morral, A. Radenovic, A. Kis, *ACS Nano* **2015**, 9, 4611.

[29] I. Bilgin, F. Liu, A. Vargas, A. Winchester, M. K. L. Man, M. Upmanyu, K. M. Dani, G. Gupta, S. Talapatra, A. D. Mohite, S. Kar, *ACS Nano* **2015**, 9, 8822.

[30] X. Ling, Y.-H. H. Lee, Y. Lin, W. Fang, L. Yu, M. S. Dresselhaus, J. Kong, *Nano Lett.* **2014**, 14, 464.

[31] J. Chen, W. Tang, B. Tian, B. Liu, X. Zhao, Y. Liu, T. Ren, W. Liu, D. Geng, H. Jeong, H. Shin, W. Zhou, K. Loh, *Adv. Sci.* **2016**, 3, 1500033.

[32] Y.-H. Lee, L. Yu, H. Wang, W. Fang, X. Ling, Y. Shi, C.-T. Lin, J.-K. Huang, M.-T. Chang, C.-S. Chang, M. Dresselhaus, T. Palacios, L.-J. Li, J. Kong, *Nano Lett.* **2013**, 13, 1852.

[33] S. Wang, Y. Rong, Y. Fan, M. Pacios, H. Bhaskaran, K. He, J. Warner, *Chem. Mater.* **2014**, 26, 6371.

[34] J. Wu, H. Schmidt, K. Amara, X. Xu, G. Eda, B. Özyilmaz, *Nano Lett.* **2014**, 14, 2730.

[35] H. Schmidt, S. Wang, L. Chu, M. Toh, R. Kumar, W. Zhao, A. H. Neto, J. Martin, S. Adam, B. Özyilmaz, G. Eda, *Nano Lett.* **2014**, 14, 1909.

[36] J. Zhang, H. Yu, W. Chen, X. Tian, D. Liu, M. Cheng, G. Xie, W. Yang, R. Yang, X. Bai, D. Shi, G. Zhang, *ACS Nano* **2014**, 8, 6024.

[37] Y. Wan, H. Zhang, K. Zhang, Y. Wang, B. Sheng, X. Wang, L. Dai, *ACS Appl. Mater. Interfaces* **2016**, 8, 18570.

[38] H. Phan, Y. Kim, J. Lee, R. Liu, Y. Choi, J. Cho, C. Lee, *Adv. Mater.* **2017**, 29, 1603928.

[39] J. Jeon, S. Jang, S. Jeon, G. Yoo, Y. Jang, J.-H. Park, S. Lee, *Nanoscale* **2014**, 7, 1688.

[40] Z. Tu, G. Li, X. Ni, L. Meng, S. Bai, X. Chen, J. Lou, Y. Qin, *Appl. Phys. Lett.* **2016**, 109, 223101.

[41] W. Chen, J. Zhao, J. Zhang, L. Gu, Z. Yang, X. Li, H. Yu, X. Zhu, R. Yang, D. Shi, X. Lin, J. Guo, X. Bai, G. Zhang, *J. Am. Chem. Soc.* **2015**, 137, 15632.

[42] Y. Gong, G. Ye, S. Lei, G. Shi, Y. He, J. Lin, X. Zhang, R. Vajtai, S. T. Pantelides, W. Zhou, B. Li, P. M. Ajayan, *Adv. Funct. Mater.* **2016**, 26, 2009.

[43] S. Wang, M. Pacios, H. Bhaskaran, J. H. Warner, *Nanotechnology* **2016**, 27, 085604.

[44] H. Zhou, C. Wang, J. C. Shaw, R. Cheng, Y. Chen, X. Huang, Y. Liu, N. O. Weiss, Z. Lin, Y. Huang, X. Duan, *Nano Lett.* **2015**, 15, 709.

[45] Z. Yan, J. Lin, Z. Peng, Z. Sun, Y. Zhu, L. Li, C. Xiang, L. E. Samuel, C. Kittrell, J. M. Tour, *ACS Nano* **2012**, 6, 9110.

[46] G. Lu, T. Wu, Q. Yuan, H. Wang, H. Wang, F. Ding, X. Xie, M. Jiang, *Nat. Commun.* **2015**, 6, 6160.

[47] W. Park, J. Baik, T.-Y. Kim, K. Cho, W.-K. Hong, H.-J. Shin, T. Lee, *ACS Nano* **2014**, 8, 4961.

[48] Q. Ji, Y. Zhang, T. Gao, Y. Zhang, D. Ma, M. Liu, Y. Chen, X. Qiao, P.-H. Tan, M. Kan, J. Feng, Q. Sun, Z. Liu, *Nano Lett.* **2013**, 13, 3870.

[49] D. Sercombe, S. Schwarz, D. O. Pozo-Zamudio, F. Liu, B. J. Robinson, E. A. Chekhovich, Tartakovskii, II, O. Kolosov, A. I. Tartakovskii, *Sci. Rep.* **2013**, 3, 3489.

[50] Y. Yoo, Z. P. Degregorio, J. E. Johns, *J. Am. Chem. Soc.* **2015**, 137, 14281.

[51] S. Xie, M. Xu, T. Liang, G. Huang, S. Wang, G. Xue, N. Meng, Y. Xu, H. Chen, X. Ma, D. Yang, *Nanoscale* **2015**, 8, 219.

[52] M. M. Furchi, A. Pospischil, F. Libisch, J. Burgdörfer, T. Mueller, *Nano Lett.* **2014**, 14, 4785.

[53] A. Pezeshki, S. Shokouh, T. Nazari, K. Oh, S. Im, *Adv. Mater.* **2016**, 28, 3216.

[54] P. Jeon, S.-W. Min, J. Kim, S. Raza, K. Choi, H. Lee, Y. Lee, D. Hwang, H. Choi, S. Im, *J. Mater. Chem. C* **2015**, 3, 2751.

[55] Y. Deng, Z. Luo, N. J. Conrad, H. Liu, Y. Gong, S. Najmaei, P. M. Ajayan, J. Lou, X. Xu, P. D. Ye, *ACS Nano* **2014**, 8.

[56] C.-H. Lee, G.-H. Lee, A. M. van der Zande, W. Chen, Y. Li, M. Han, X. Cui, G. Arefe, C. Nuckolls, T. F. Heinz, J. Guo, J. Hone, P. Kim, *Nat. Nanotechnol.* **2014**, 9, 676.

[57] J. Zhang, J. Wang, P. Chen, Y. Sun, S. Wu, Z. Jia, X. Lu, H. Yu, W. Chen, J. Zhu, G. Xie, R. Yang, D. Shi, X. Xu, J. Xiang, K. Liu, G. Zhang, *Adv. Mater.* **2016**, 28, 1950.

[58] K. Kośmider, J. Fernández-Rossier, *Phy. Rev. B* **2013**, 87, 75451.

[59] X. Hong, J. Kim, S.-F. Shi, Y. Zhang, C. Jin, Y. Sun, S. Tongay, J. Wu, Y. Zhang, F. Wang, *Nat. Nanotechnol.* **2014**, 9, 682.

[60] Y. Yu, S. Hu, L. Su, L. Huang, Y. Liu, Z. Jin, A. A. Purezky, D. B. Geohegan, K. Kim, Y. Zhang, L. Cao, *Nano Lett.* **2015**, 15, 486.

[61] M. M. Furchi, D. K. Polyushkin, A. Pospischil, T. Mueller, *Nano Lett.* **2014**, 14, 6165.

[62] D. J. Late, B. Liu, R. Matte, V. P. Dravid, C. N. R. Rao, *ACS Nano* **2012**, 6, 5635.

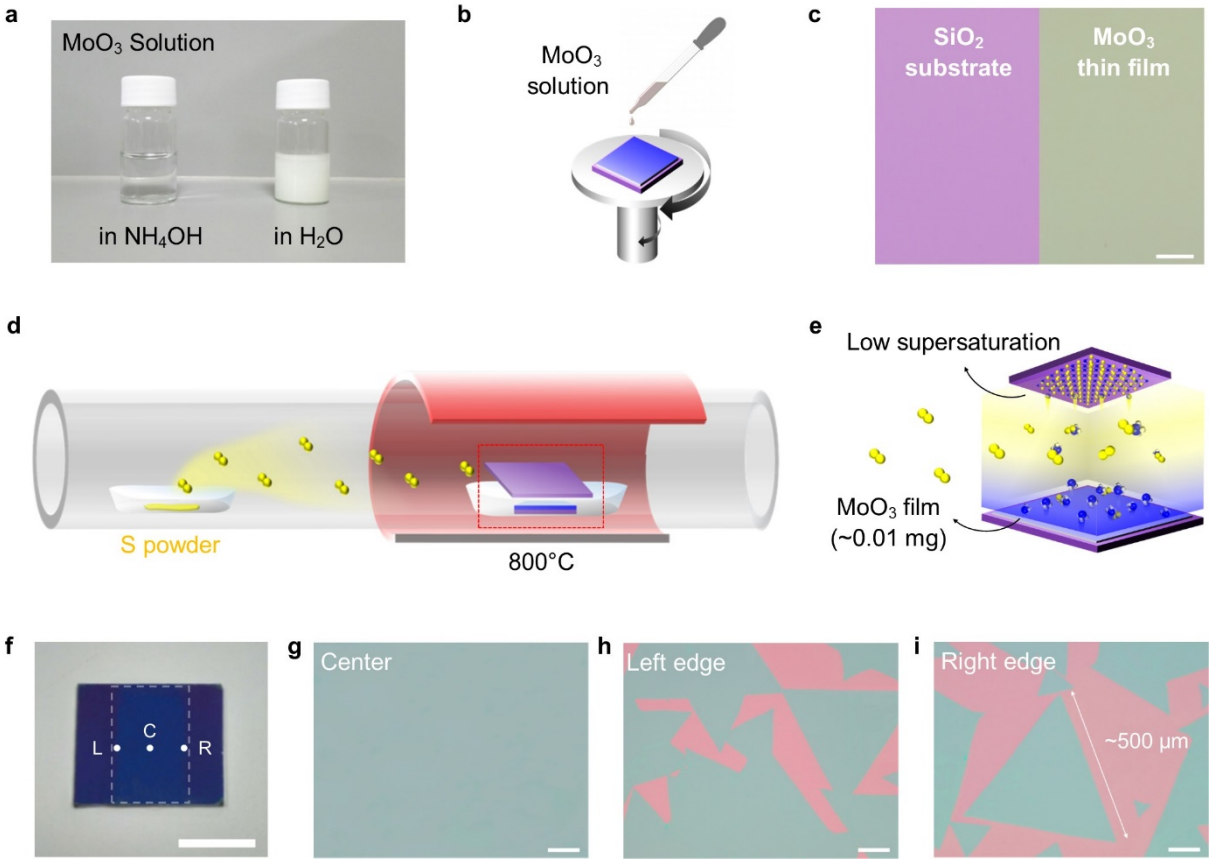

Figure 1. Low supersaturation synthesis of a MoS_2 monolayer film. a) MoO_3 solution in NH_4OH and in H_2O. **b)** Deposition of the MoO_3 film on the SiO_2 substrate by spincoating the MoO_3 solution. **c)** Optical images of the blank SiO_2 substrate and the MoO_3 film. Scale bar: 10 μm. **d)** Illustration of the synthesis process for a MoS_2 monolayer film. **e)** Enlarged diagram of the source substrate and the target substrate in the red-dashed box shown in d). **f)** Optical image of the as-grown MoS_2 film. The film was grown mainly on the area directly exposed to MoO_3 inside the crucible. Scale bar: 1 cm. **g-i)** Typical images of MoS_2 crystals grown in the center, the left edge, and the right edge of the substrate, respectively, as marked in (f). Scale bars: 100 μm.

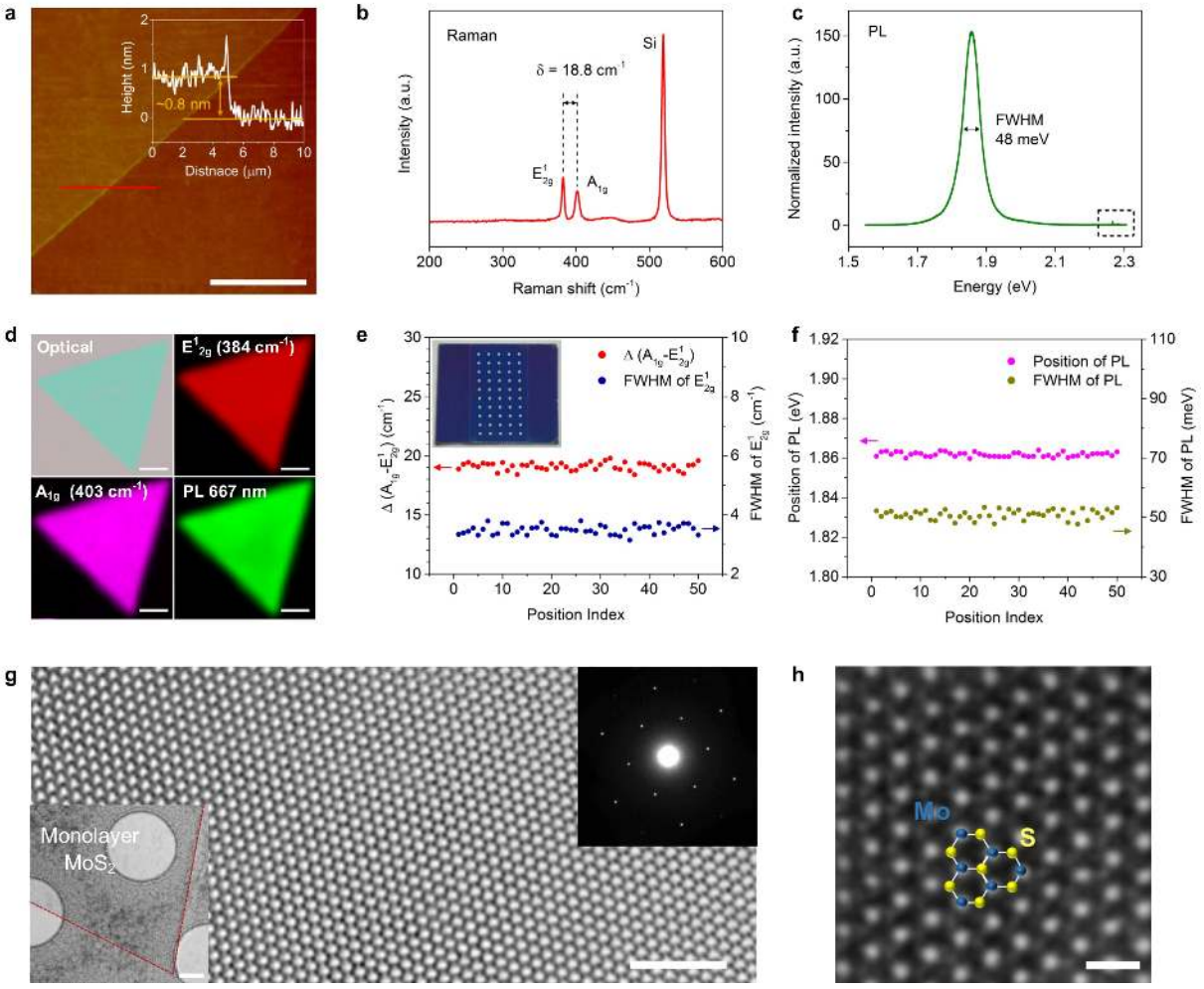

Figure 2. Characterization of the MoS_2 monolayer. a) AFM image of a MoS_2 monolayer crystal. The inset shows that the thickness of the crystal corresponds to a MoS_2 monolayer. Scale bar: 10 μm. **b)** Raman spectrum of the MoS_2 monolayer. **c)** PL spectrum of the MoS_2 monolayer normalized to the intensity of the A_{1g} peak. The Raman peaks of MoS_2 and SiO_2 in the dashed box appear negligible because the PL peak is extremely intense. **d)** Optical image of a MoS_2 crystal, and the corresponding Raman and PL mapping images. Scale bars: 20 μm. **e)** The frequency difference between the E^1_{2g} and A_{1g} peaks, and the FWHM of the E^1_{2g} peak collected from 50 different locations across the substrate (inset). **f)** The peak energy (eV) and the FWHM of the PL spectra measured from the same locations as shown in (e). **g)** High-resolution TEM image of a MoS_2 monolayer. Scale bar: 2 nm. Left inset: crystal on the TEM grid. Scale bar: 500 μm. Right inset: SAED image confirming the hexagonal structure. **h)** ADF-STEM image representing the defect-free hexagonal structure of the monolayer. The bright spots are Mo atoms, and the grey spots are two stacked S atoms. Scale bar: 0.5 nm.

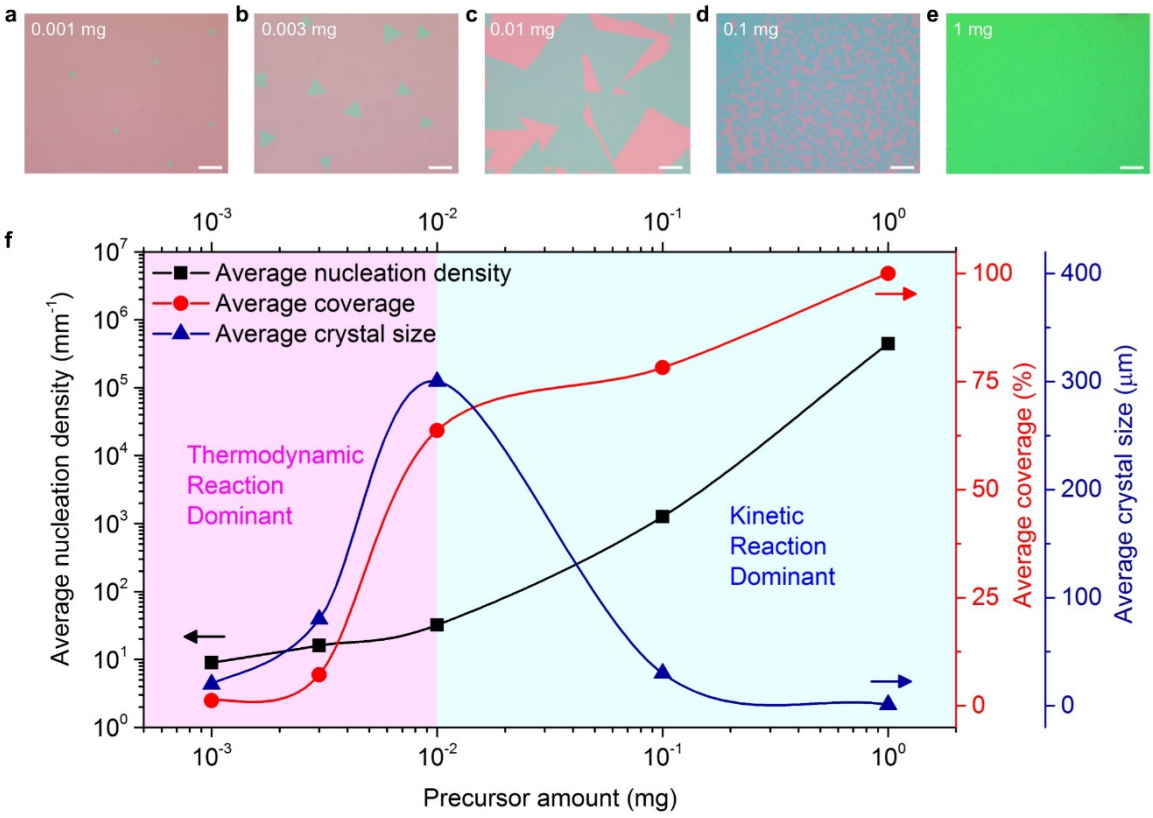

Figure 3. The effect of the supersaturation level on the growth of the monolayer. a-e) Optical images of the crystals grown with different amounts of MoO_3 ranging from 0.001 to 1 mg. The images were taken at the center of each substrate. Scale bars: 100 μm. **f)** Average nucleation density, average coverage, and average crystal size as a function of the amount of MoO_3 precursor.

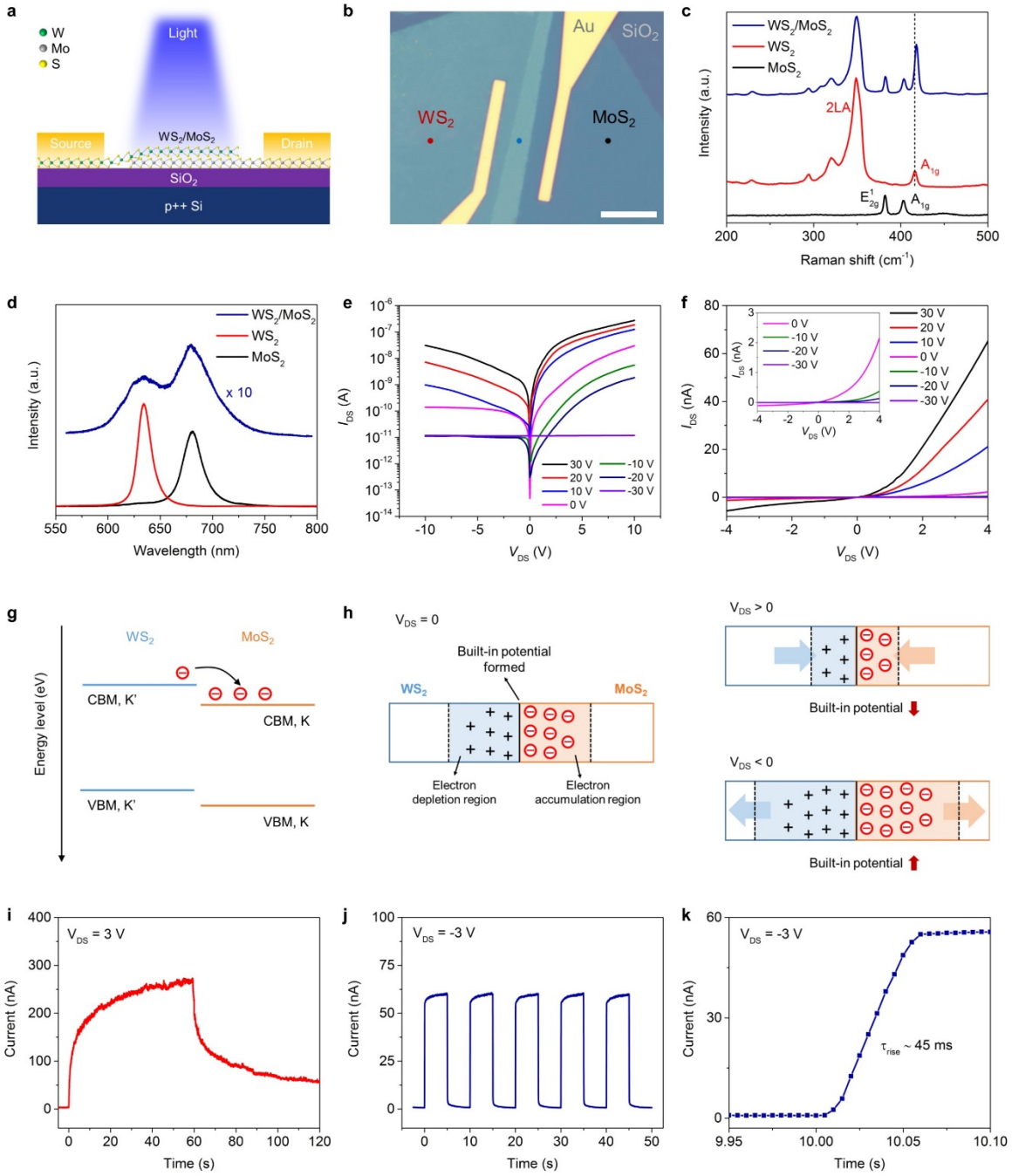

Figure 4. MoS_2/WS_2 heterojunction devices. a) Schematic of the MoS_2/WS_2 heterojunction devices. **b)** Optical image of the MoS_2/WS_2 heterojunction device. Scale bar:10 μm. **c)** Raman spectra measured at the junction (blue), on the WS_2 crystal (red), and on the MoS_2 crystal (black). **d)** PL spectra measured from the same spot in (c). **e)** I-V curves of the heterojunction device at different gate voltages on a logarithmic scale. **f)** I-V curves of the heterojunction device on a linear scale. The inset shows an enlarged plot for below a gate voltage of 0 V. **g)** Illustration of the band alignment of a MoS_2/WS_2 heterojunction. When the heterojunction

forms, electrons on the WS_2 side are transferred to the MoS_2 side due to the difference in energy level. **h)** Schematic of the heterojunction at zero bias, at $V_{DS} > 0$, and at $V_{DS} < 0$. The size of the built-in potential varies according to the bias. **i)** Photoresponse of the heterojunction device at $V_{DS} > 0$. The blue laser (450 nm, 0.76 mW/cm^2) was incident on the junction for 60 s. **j)** Photoresponse at $V_{DS} < 0$. Light was illuminated for 5 s with a period of 10 s. **k)** The rise time was measured by the enlarged plot when the light was on.

Large-scale and highly-crystalline molybdenum disulfide monolayers are synthesized by a solution-processed precursor deposition technique. The low supersaturation level under a thermodynamically stable condition reduces the nucleation density dramatically and thus produces clean monolayer films with a grain size up to 500 μm. The MoS_2/WS_2 heterojunction device based on this synthesis procedure shows a fast response time with a significantly high photoresponsivity.

Keyword: transition metal dichacogenides, two-dimensional materials, chemical vapor deposition, heterojunctions, photodetectors

J. W. Lee, S. Pak, P. Giraud, Y. -W. Lee, Y. Cho, J. Hong, A. -R. Jang, H. Y. Jeong, H. S. Shin, L. G. Occhipinti, S. M. Morris, S. Cha*, J. I. Sohn*, J. M. Kim

Thermodynamically stable synthesis of large-scale and highly-crystalline transition metal dichalcogenide monolayers and their unipolar n-n heterojunction devices